Three-Dimensional Imaging and Satellite Attitude Estimation Using Pulse Laser Illumination and a Remote Ultra-Low Light Imaging (RULLI) Sensor for Space Situational Awareness (SSA)

Michael C. Roggemann[1], Kris Hamada[2], Kim Luu[3], Venkata S. Rao Gudimetla[3],
Randy F. Cortez[2], L. William Bradford[2], David C. Thompson[4], Robert Shirey[4]

Abstract

The remarkable temporal resolution of the Remote Ultra-Low Light Imaging (RULLI) sensor developed by Los Alamos National Laboratory has led to interest in exploiting this capability to perform 3-D imaging of satellites for improved Space Situational Awareness (SSA). Such a system would require a pulsed laser illuminator combined with an adaptive optics system. We have developed a simulation of such a system and present a discussion of the model and preliminary results. These results show that 3-D imaging is a potentially powerful tool for understanding the orientation and configuration of satellites.

Introduction

Remote Ultra-Low Light Imaging (RULLI) detectors have been developed at Los Alamos National Laboratories (LANL) for the purposes of two dimensional (2-D) passive imaging and three-dimensional (3-D) active imaging at visible wavelengths [Priedhorsky, 1996a; Priedhorsky, 1996b; Ho, 1999; Priedhorsky, 2005]. The RULLI detector combines photon-limited detection with a precise timing capability. Physically, a RULLI detector consists of photo-cathode, followed by a micro channel plate gain stage. The electron cloud generated by the gain stage falls on a crossed-delay line detection system, and the electronics associated with this readout mechanism account for both the photon-limited nature of the detection and the high degree of temporal resolution. The RULLI detector has neither pixels nor frames; the data stream output by the RULLI detector is a sequence of photo-electron locations and arrival times. Both position and time data have very high resolution, but electron optics and other effects give rise to point spread functions in space and time with widths equivalent to ~100 microns for a 40 mm diameter detector and an absolute time resolution of ~100 ps. The RULLI detector also has extremely low dark current but has a relatively low saturation count rate of about 10^6 photo-electrons/second. These properties of the RULLI detector make it a favorable option for both passive 2-D imaging of very dim objects and 3-D imaging using pulsed laser illumination of targets. In this paper we present a model for a 3-D imaging system based on pulsed laser illumination and a receiver imaging telescope equipped with adaptive optics. Resolution in the range direction is provided by the pulsed nature of the laser and precise timing of the returned pulses, and resolution in the orthogonal plane is provided by the adaptive optics of the receiver telescope.

The degree of temporal resolution provided by the RULLI detector offers the opportunity to perform time-resolved active imaging in a manner which provides unprecedented resolution in the range dimension. We have used a well-developed model for wave propagation through turbulence and the

[1] Michigan Technological University, Houghton, MI, and Pacific Defense Solutions, Kihei, HI
[2] Pacific Defense Solutions, Kihei, HI
[3] Air Force Research Laboratory, Maui Space Surveillance Site, Kihei, HI
[4] Los Alamos National Laboratory, Los Alamos, NM

time-resolved RULLI detector model to simulate 3-D imaging with a RULLI detector, and results are presented here. These models can be used to efficiently study new systems and applications using RULLI detectors for time-resolved imaging applications. In addition to developing the models, we have also developed data processing algorithms that allow extremely accurate estimation of satellite orientation by matching a 3-D model of the satellite to the 3-D data. Results from these efforts are also presented here.

The remainder of this paper is organized as follows. The RULLI detector model is presented in the next section. The propagator and receiver models are discussed next, followed by a discussion of the satellite orientation processing. Results are presented, and conclusions are drawn in the final section.

RULLI Detector Model

We now describe the RULLI detector model. The input to the RULLI detector model is the classical image intensity $I(x_I, y_I; t_n)$, as computed using the techniques of Fourier optics [Goodman, 2005], where (x_I, y_I) is a discrete image plane coordinate and t_n represents time of the nth time step of the simulation which has temporal time steps given by Δt, which represents the temporal resolution of the detector model. The mean number of photo-electron counts associated with this realization of the classical image intensity is represented by $\overline{K}$. $I(x_I, y_I; t)$ is generally sampled at the Nyquist angular sampling rate for the aperture $\frac{\lambda}{(2D)}$, where λ is the wavelength and D is the telescope diameter. $\overline{K}$ is generally computed from radiometric considerations for the problem at hand, but it can also be set arbitrarily for parametric studies. If we let N be the number of time steps the simulation is to be run, then $N\Delta t$ is the total duration of the observation. The output of the RULLI model is three vectors, one each for the (x_I, y_I) location, and a third column holding the time of arrival of each recorded photo-event.

It should be noted that for a real RULLI detector $\overline{K}/\Delta t$, which has units of photo-counts per second, should never exceed the saturation rate of detector, which is on the order of 10^6 photo-events per second. In simulation, meeting this requirement can lead to exceedingly long run times, since $\overline{K} \ll 1$ under many realistic conditions. It should be noted that as a result, the value of $\overline{K}$ is sometimes set artificially high in simulation. There is very little practical impact to the performance of the simulation, since the photo-events are still Poisson distributed. When more than one photo-event per time step Δt arises, the time interval Δt is split into $\Delta t/K$ smaller time steps, where K is the number of photo-events in the frame. One photo-event is assigned to each small time step, and the order in which the photons arrived is randomized. The value of Δt presently implemented in the simulation is 0.33 ns, at least two orders of magnitude larger than the smallest detectable time step which a real RULLI detector could provide, so this issue of exceeding the temporal resolution characteristics of the RULLI rarely, if ever, arises in practice. We now discuss the 3-D propagator and receiver models.

Propagator and Receiver Models

RULLI data obtained by scattering a pulsed illuminating laser on a distant object can be processed to make a three dimensional (3-D) rendering of the surface scatterer locations which represents the shell of the outer surface of the target. In this section we describe the 3-D imaging model and present representative results. Notionally, a RULLI-based 3-D imaging system would work as follows:

1. A short laser pulse is fired at the target.

2. The pulse propagates to the target through the atmosphere and then free space, so that the beam falling on the target is affected by atmospheric turbulence effects.
3. As the pulse passes by the target, light is scattered from the surface of the target, and some of this light propagates back in the direction of the receiver. The temporal and spatial profile of the scattered pulse is affected by the object, and as a result, the back scattered light contains information about both the reflectivity and depth along the direction of propagation of the pulse of the surface scatterers of the target.
4. Some of the backscattered light propagates back through the atmosphere and is intercepted by the receiver telescope.
5. The RULLI detector model converts the classical image into a stream of photo-electron locations and times of arrivals. This stream of time-resolved data can be processed to render both 2-D and 3-D images.

Most targets of interest have depth along the line of sight greater than the linear pulse length, and hence the duration of the returned pulses will be greater than the outgoing pulse, thus providing information about the depth of the target surface scatterers. We are presently modeling the targets as Lambertian scatterers, and hence, the backscattered radiation is spatially incoherent. Some of the backscattered radiation travels in the direction of the receiver and is intercepted. To develop the model we have assumed the receiver is the AEOS system with the AO system operating and that the target is sufficiently bright due to solar illumination to provide good signal-to-noise ratio (SNR) in the wave front sensor (WFS) and tracker channels. A conventional, adaptive optics compensated image at the laser wavelength is formed and falls on the RULLI detector. The image plane is assumed to be spectrally isolated from the solar illumination scattered from the satellite and other sources of background radiation by a very narrow spectral filter centered on the laser wavelength. By most standards the image falling on the RULLI must always be an exceedingly dim image due to the stringent saturation limitations of the RULLI detector.

To simulate 3-D imaging the target is "sliced" in the depth dimension into non-overlapping elements $c\tau_R/2$ in length, where c is the speed of light, τ_r is the temporal resolution of the RULLI detector, and the factor of one half accounts for the two-pass nature of the propagation to and from the target. Imaging with a RULLI detector in this manner can be reasonably considered to be a highly time-resolved incoherent imaging system. An incoherent image with the appropriate time delay to account for the round trip distance of each slice and the RULLI detector model then determines the random locations and times of arrival of the photo electrons. The resulting stream of (x, y, t) data describing each photo-event can be processed to arrange 3-D renderings of the object which was measured.

The illuminating laser beam is modeled as a pulsed laser with a wavelength of λ = 532 nm. The pulse duration of the laser was set at $T_P = 8$ ps, and the repetition rate was set at 1 MHz. This beam is passed through a $D = 60$ cm diameter aperture for the uplink. The e^{-1} radius of the field strength which passes 95% of the power of a Gaussian TEM_{00} beam is $w_0 = \frac{1}{1.224}\left(\frac{D}{2}\right) = 24.5$ cm. Since diffraction and turbulence effects will not be sufficient to broaden the beam enough to fully illuminate the target, it is necessary to diverge the outgoing beam at the pupil. This is accomplished in the model with a negative lens placed in the pupil of the transmitter. The relationship between the divergence angle θ_D and the

focal length of this negative lens f_l is $f_l = -\left(\frac{D}{2}\right)\left(\frac{1}{\theta_D}\right)$. The expression for the electric field due to the beam leaving the aperture is thus

$$E(x, y, z = 0) = E_0 \exp\left[-\left(x^2 + y^2\right)\Big/ w_0^2\right] \exp\left[-j\frac{k}{2f_l}\left(x^2 + y^2\right)\right],$$

where E_0 is the peak strength of the field and $k = 2\pi/\lambda$.

While the free space propagation characteristics of Gaussian beams are well understood [Verdeyen, 1995; Ishimaru, 1978], atmospheric turbulence-induced errors cause detrimental effects on the propagating beam [Beland, 1993]. These effects include (1) broadening - the transmitted beam is broadened more than would be predicted by diffraction in free space alone, distributing the energy over a wider area; (2) wandering - the beam appears to "wander" in the sense that the centroid of the intensity pattern at the target or receiver plane will move randomly; and (3) speckling - on short time scales the intensity distribution will be "speckled", exhibiting high spatial frequency modulation in the intensity pattern. The long time average e^{-1} radius of the intensity pattern $\left\langle \rho_L^2 \right\rangle$ after propagation through a turbulent path of length L has been analyzed, with the result [Beland, 1993]

$$\left\langle \rho_L^2 \right\rangle = w^2(z) + \frac{4L^2}{(k\rho_0)^2},$$

with

$$\rho_0 = \left[1.46k^2 (\sec\theta_z) \int_0^L C_n^2(\eta)\left(1 - \eta/L\right)^{5/3} \mathrm{d}\eta\right]^{-3/5},$$

where θ_z is the zenith angle, $C_n^2(\eta)$ is the structure constant of the turbulence as a function of altitude, η, and $w(z)$ is the radius of the beam waist a distance z from the aperture [Verdeyen, 1995; Ishimaru, 1978]. The present case of viewing at $\theta_z = 0$ deg, through the Maui3 turbulence profile yields $\rho_0 = 8.1$ cm. As an example, at the top of the atmosphere, the first term in the expression for $\left\langle \rho_L^2 \right\rangle$, which is due to diffraction effects, evaluates to $w^2(z) =$ 0.0602, and the second term in the expression for $\left\langle \rho_L^2 \right\rangle$, which is due to turbulence induced broadening, evaluates to $\frac{4L^2}{(k\rho_0)^2}$ = 0.0016, which yields a theoretical value for the e^{-1} radius of the intensity pattern of 24.9 cm. We have tested this simulation extensively and found that it matches theory well [Sergeyev, 2008].

In a pulsed laser illumination system the length of the pulse is cT_P, where c is the speed of light. In practice it is often the case that $cT_P \ll L_T$, where L_T is the length of the target along the direction of propagation of the laser. As a result, the duration of the returned pulse is generally much longer than the duration of the transmitted pulse. This is due to the fact that as the leading edge of the transmitted pulse falls on the surface of the target closest to the transmitter light is immediately scattered back in the direction of the receiver, and this process continues until the trailing edge of the pulse has passed by the target.

We now discuss the down welling beam. We have assumed that the surface of the target is Lambertian, or optically rough [Goodman, 1985], so that the spatial coherence of the illuminating beam is that of a spatially incoherent but spectrally narrow source. A Lambertian target is "optically rough" in the sense that the complex field reflectivity of the scattering surface contains a random phase term, and this random phase is uniformly distributed on $(-\pi, \pi)$ [Goodman, 1985]. This is the model of a spatially incoherent, narrow spectral band source. As a result, the images formed by the imaging system are incoherent but highly time-resolved. In this paradigm the angular resolution of the images is controlled by the combination of atmospheric seeing and AEOS/AO system performance, while resolution along the line of sight is controlled by the RULLI detector temporal resolution and timing issues associated with the pulsed laser illuminator. At each time step an incoherent image falls on the surface of the RULLI detector. The RULLI detector model randomly assigns photo-events to locations according to the Poisson distribution with a normalized version of the incoherent image serving as the rate function. In addition, the projected area of each scattering surface in the direction of the receiver is foreshortened by a factor of $\cos\phi$, where ϕ is the angle between a line connecting the target and the receiver, and the local surface normal of the object. In calculations of radiometric power transfer in optical systems it is necessary to account for this foreshortening of the area of the target but including a multiplicative factor of $\cos\phi$ in the calculations of the projected area for power transfer calculations and a factor of $\sqrt{\cos\phi}$ in calculations involving field quantities.

A wave optics propagator [Brennan, 2006] is used to move the illuminating field up through the atmosphere. The turbulence volume is modeled using 10 discrete layers – each layer is a phase-only function which represents the statistics of Kolmogorov turbulence, and wave optics propagation is used to move from screen-to-screen in both directions. The phase screen generator is widely available [Brennan, 2006], and the Maui3 turbulence profile was used. The Fried parameter for each layer was calculated by integrating through the turbulence strength profile starting at the top of the atmosphere, integrating in the direction of the receiver. A phase screen was placed in the pupil of the telescope, and the remainder were equally spaced above the aperture.

After the two-pass propagation, a classical field falls upon the telescope aperture. This field is converted to a simulated RULLI data stream in the following manner. The classical intensity image associated with the field intercepted by the aperture is computed using standard Fourier optics techniques [Goodman, 1996] for each time slice. The residual aberration affecting the instantaneous point spread function (PSF) was computed by ray tracing from the object, through the current state of the atmosphere to the pupil, and then through the AO model. This PSF was convolved with the appropriate slice of the object to make an instantaneous image of that slice, which was input to the RULLI detector model. The temporal resolution of the receiver model for the results presented below is 0.33 ns, yielding a range resolution of approximately 5 cm for the system. A 3-D rendering of the ARGOS satellite was obtained and sliced along the line of sight between the sensor and the satellite into layers 5 cm thick. A series of laser pulses were propagated through the atmosphere, from the top of the atmosphere to the target plane, and used to illuminate the satellite. The intensity illuminating the satellite was spatially varying. The life time of the atmospheric turbulence was set at 10 ms, so that every 10 ms a new realization of the 3-D volume of the atmosphere was obtained. The laser was run at a pulse rate of 100,000 pulses per second, and the mean count rate at the receiver was set at 5 photo-electrons per pulse. Data was simulated for a time interval of 0.5 s, so that the mean number of photo-electrons detected during this time is 250,000. The images were also sampled in object space at the Nyquist angular sampling rate for the aperture and wavelength of 73.89 nRad. The range of the target was 9.76×10^5 m. The RULLI data was assembled into both a 2-D image and a 3-D object rendering using the approach described above,

and the results are shown in Fig. 1. Inspection of Fig. 1 shows that that excellent 2-D and 3-D renderings of objects can be created from RULLI measurements.

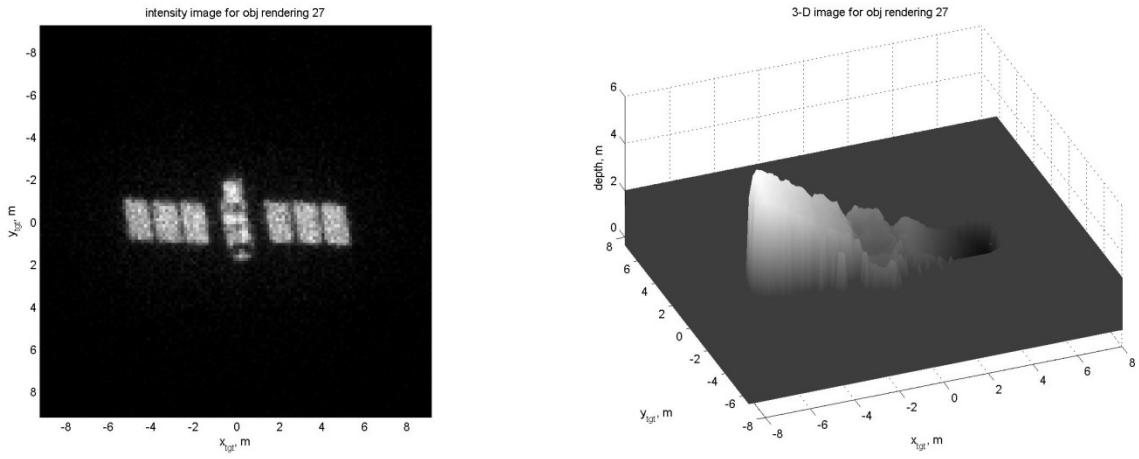

(a) (b)

Figure 1. (a) 2-D image created from the RULLI data; (b) 3-D object rendering obtained from the simulated RULLI data

Satellite Orientation Estimation

jTrack is a software utility developed by the United States Air Force Research Laboratory (AFRL) to review SSA imagery quickly and easily. jTrack also allows analysts to manually determine the orientation of a satellite by overlaying a model directly on the images in a Model Overlay window, shown in Fig. 2. The Model Overlay window size is equal to the field of view of the sensor used to gather the data. Orienting the model to the measured image helps the analyst with change detection (comparing any new features that show up in the imagery versus what the model has), determine the state of satellite (whether it is operational or not by looking at solar panel alignment with respect to the sun), and determine where a satellite is generally pointing. Satellite ground pointing of 2-D imagery is determined in jTrack by orientating the satellite model to the imagery for selected frames also known as key frames. During the orientation for the selected key frames, an interpolation algorithm is continuously updating the model orientation for non key frames. Once the analyst determines to have a good orientation, a data spreadsheet containing satellite pointing latitude and longitude is created. We have made modifications to jTrack to visualize and analyze simulated 3-D data.

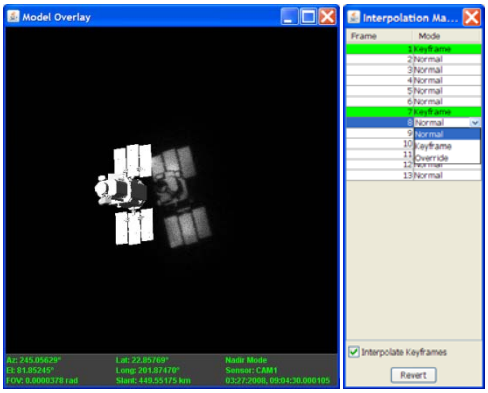

Figure 2. Example of Model Overlay and Interpolation Manager Windows.

By using the time of arrival data and the spatial information about where the photo-events arrived, it is possible to create a 3-D representation of the receiver output which we refer to as a "photon cast". The photon cast contains information about the locations of the surface scatterers on the object in all three dimensions. An example photon cast is shown in Fig. 3.

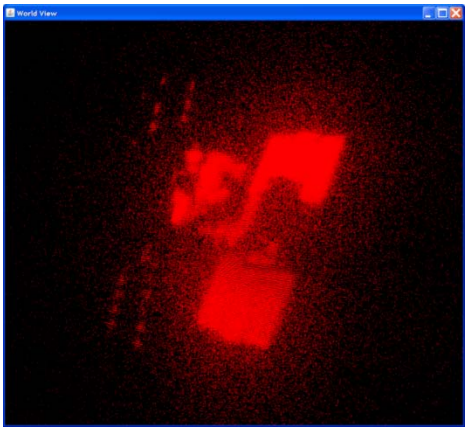

Figure 3. Example photon cast data.

In jTrack, the 3-D photon cast is attached to the sensor model and translated in slant range to the satellite model. The capability to calculate the distance between points on the model and points on the photon cast was added to jTrack and used to estimate the proper orientation of the model to the simulated measurements. An example of this capability is shown in Fig. 4, where the photon cast is shown in red, and the model is shown in gray. Being able to calculate this distance provides a numerical metric for analysts to measure the dimensions of a satellite without having any prior knowledge of a satellite. It is also possible to compare measurements of the satellite to known dimensions of a satellite. The ability to load 3-D photon cast data now provides the analyst the capability to orient a satellite model with 3-D photon cast data which may increase the accuracy of determining where a satellite was pointing.

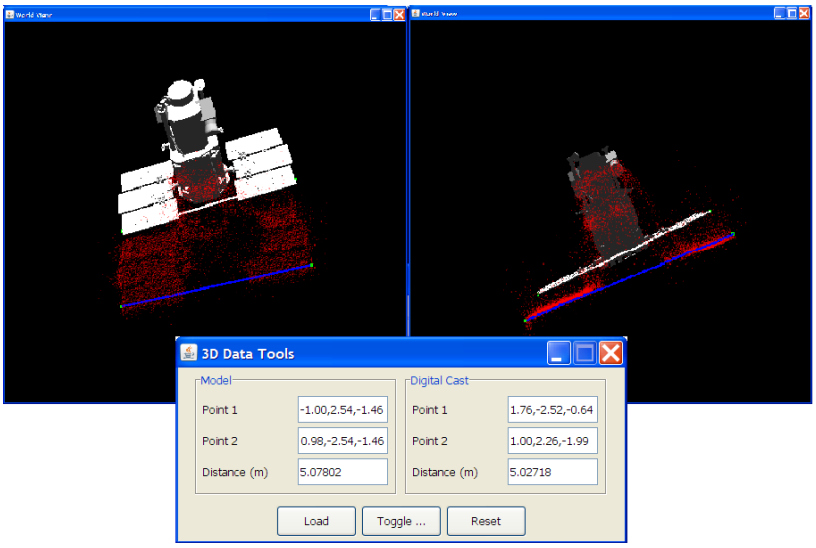

Figure 4. Example of point to point measurements calculations. The World View Window shows a different orientation of the satellite model and 3-D photon cast.

Results

The model orientation was done on a simulated single pass of the Quickbird satellite fixated at a 5 different ground points, therefore giving a total of 5 orientation comparisons to be done. The analyst doing the orientation had no prior knowledge of the 5 ground points selected. For each satellite orientation, the analyst loaded 13 images with the satellite having a maximum slant range of 645.0 km and having a culmination slant range of 450.0 km. The performance of the orientation estimation process was evaluated for three different ways of using the data: rendering it as a 2-D intensity image, using 3-D photon cast data, and by spatially binning the 3-D photon cast data to reduce the effects of photon noise.

In order to do the model orientation to the 2-D image or 3-D photon cast, every other frame was selected as a key frame. For the other frames in the satellite pass, jTrack's model interpolation algorithm was used. Selecting every other frame allows the interpolation algorithm to interpolate one frame between each key frame rather than interpolating multiple frames between each key frame, thereby reducing the error introduced by the interpolation algorithm. Ideally, setting each frame to a key frame will give a measurement based on the analyst's ability to do a model orientation and not introduce any interpolation error but will increase the time spent by an analyst performing a model orientation.

Once all orientations (2-D Images, 3-D All Points Photon Cast, and 3-D Binned Photon Cast) have been completed, the pointing distance error for each frame X, the mean pointing distance error $\bar{X}$ and the standard deviation of the pointing distance error σ was calculated. The unit of measurement for these calculations is in degrees. The distance error between the actual pointing location in the model and the estimated pointing location is represented by X, with

$$X = \sqrt{\Delta x^2 + \Delta y^2}\,, \qquad \begin{array}{l} \Delta x = |actual\ latitude - measured\ latitude| \\ \Delta y = |actual\ longitude\ - measured\ longitude| \end{array}$$

and X has mean $\bar{X}$ and standard deviation σ defined by

$$\bar{X} = \frac{1}{n}\sum_{i=1}^{n} X_i\,, \qquad n = \text{Number of Frames}$$

$$\sigma = \sqrt{\frac{1}{n}\sum_{i=1}^{n}(X_i - \bar{X})^2}$$

After the mean and standard deviations for pointing distance error were calculated in degrees, the units for the pointing distance error were converted to kilometers (km), using

$$Distance\ Error\ (km) = Distance\ Error\ (degrees) * \frac{2\pi r_{equator}}{360}\ (\frac{km}{degrees}).$$

An error ellipsoid was calculated for all orientation points of a pass and for all orientations points whose frames have a slant range < 500 km. The covariance for a set of points was calculated using:

$$cov\ xy = \frac{1}{n-1}\sum_{i=1}^{n}(X_i - \bar{X})\,(Y_i - \bar{Y})\,, \quad \begin{array}{l} X = Latitude \\ Y = Longitude \end{array}$$

The mean pointing latitude and longitude positions were also calculated. From there the covariance values were added to the mean pointing angles to calculate the points of the error ellipsoid. The standard deviation for the pointing angles were also calculated. The simulations were run for five different fixation points, all on the landmass of the Hawaiian islands: (Latitude - 21.38°, Longitude - 202.013°), (Latitude - 21.38°, Longitude - 202.013°), (Latitude - 21.42603°, Longitude - 202.2473°), (Latitude - 22.03473°, Longitude - 200.2254°), and (Latitude - 19.72237°, Longitude - 204.9448°).

The results of this study are presented in Tables 1 through 4, which consolidate all of the data from all five simulated passes. Table 1 shows the pointing distance errors in units of degrees, and Table 2 shows the pointing distance errors in units of kilometers for all the data. Tables 3 and 4 provide similar results, but with the slant range of the targets from the sensor included in the table.

Table 1. Pointing distance error for the 5 combined Quickbird orientations, units in degrees.

5 Quickbird Orientations	All Frames		Key Frames	
	Mean	Std	Mean	Std
2-D Images	0.1518562	0.08453994	0.16096309	0.10026135
3-D All Points	0.1111668	0.05462057	0.10658302	0.05410786
3-D Binned	0.1655650	0.06342982	0.16189306	0.06137551

Table 2. Pointing distance error for the 5 combined Quickbird orientations, units in kilometers

5 Quickbird Orientations	All Frames		Key Frames	
	Mean	Std	Mean	Std
2-D Images	16.904554	9.41094031	17.9183233	11.16103880
3-D All Points	12.375025	6.08033227	11.8647636	6.02325805
3-D Binned	18.430608	7.06087331	18.0218470	6.83228867

Table 3. Pointing distance error in relation to slant range for the 5 combined Quickbird orientations, units in degrees

5 Quickbird Orientations	Slant Range < 500 km		Slant Range > 500km, < 600 km		Slant Range > 600 km	
	Mean	Std	Mean	Std	Mean	Std
2-D Images	0.111599	0.047218	0.171949	0.068547	0.222395	0.138047
3-D All Points	0.102830	0.043953	0.120985	0.060571	0.111633	0.068609
3-D Binned	0.162028	0.062843	0.170316	0.064943	0.164300	0.067320

Table 4. Pointing distance error in relation to slant range for the 5 combined Quickbird orientations, units in kilometers

5 Quickbird Orientations	Slant Range < 500 km		Slant Range > 500km, < 600 km		Slant Range > 600 km	
	Mean	Std	Mean	Std	Mean	Std
2-D Images	12.423130	5.256326	19.141306	7.630557	24.756930	15.367330
3-D All Points	11.446930	4.892836	13.467984	6.742713	12.426900	7.637488
3-D Binned	18.036850	6.995698	18.959439	7.229365	18.289790	7.494042

Examination of Tables 1 through 4 shows that the 3-D data provides better satellite orientation estimates than either the 2-D data, or the binned 3-D data, offering a potentially significant improvement in SSA capabilities.

Conclusion

In this paper we have discussed a model for a 3-D imaging system based on a pulsed laser illuminator and a RULLI detector. We have found that, in simulation, 3-D imaging with a RULLI-based system can provide superior satellite orientation estimates compared to processing 2-D data.

References

[Brennan, 2006] Terry J. Brennan and Phillip H. Roberts, "AOTools – The Adaptive Optics Toolbox for use with MATLAB", the Optical Sciences Company, Anaheim, CA, 2006. (available on-line at: http://www.tosc.com/downloads/AOToolsUG.pdf)

[Beland, 1993] R. R. Beland, "Propagation through atmospheric turbulence", Chapter 2, Volume 2, IR/EO Handbook, SPIE Optical Engineering Press, Bellingham, WA, 1993.

[Goodman, 1985] J. W. Goodman, *Statistical Optics*, Wiley-Interscience, New York, 1985.

[Goodman, 1996] J. W. Goodman, *Introduction to Fourier Optics, 3rd Edition*, McGraw Hill Company, Inc., New York, 1996.

[Ho, 1999] Cheng Ho, Kevin L. Albright, Alan W. Bird, Jeffrey Bradley, Donald E. Casperson, Miles Hindman, William C. Priedhorsky, W. Robert Scarlett, R. Clayton Smith, James Theiler, and S. Kerry Wilson, "Demonstration of literal three-dimensional imaging", *Appl. Opt*., vol. 38, p1833-1840, 1999.

[Ishimaru 1978] A. Ishimaru, "The beam wave case and remote sensing", in *Laser Beam Propagation in the Atmosphere*, Ed. J. W. Strohbehn, Vol. 25, Topics in Applied Physics, Springer-Verlag, Berlin, 1978.

[Priedhorsky, 1996a] William C. Priedhorsky, R. Clayton Smith, and Cheng Ho, "Laser ranging and mapping with a photon-counting detector", *Appl. Opt*., vol. 35, p441-452, 1996.

[Priedhorsky, 1996b] William C. Priedhorsky, "Contrast and signal-to-noise ratio in long-distance starlight imaging", *Appl. Opt*., vol. 35, p4173-4179, 1996.

[Priedhorsky, 2005] William Priedhorsky and Jeffrey J. Bloch, "Optical detection of rapidly moving objects in space", *Appl. Opt*., vol. 44, p423-433, 2005.

[Sergeyev, 2008] A. V. Sergeyev, P. Piatrou, and M. C. Roggemann, "Bootstrap beacon creation for overcoming the effects of beacon anisoplanatism in a laser beam projection system", *Appl. Opt.*, vol. 47, p2399-2413, 2008.

[Verdeyen, 1995] J. T. Verdeyen, *Laser Electronics, 3rd Edition*, Prentice-Hall, Upper Saddle River, NJ, 1995.